Available online at www.sciencedirect.com
ScienceDirect
International Journal of Multiphase Flow 32 (2006) 1072–1086
International Journal of Multiphase Flow
www.elsevier.com/locate/ijmulflow

Some generic capillary-driven flows

W. Villanueva *, G. Amberg

Department of Mechanics, Royal Institute of Technology, SE-100 44 Stockholm, Sweden

Received 16 July 2005; received in revised form 7 May 2006

Abstract

This paper deals with numerical simulations of some capillary-driven flows. The focus is on the wetting phenomenon in sintering-like flows and in the imbibition of liquids into a porous medium. The wetting phenomenon is modeled using the coupled Cahn–Hilliard/Navier–Stokes system. The Cahn–Hilliard equation is treated as a system where the chemical potential is solved first followed by the composition. The equations are discretised in space using piecewise linear functions. Adaptive finite element method is implemented with an ad hoc error criterion that ensures mesh resolution along the vicinity of the interface. In the 3D case we use parallel adaptive finite element method. First, a basic wetting of a liquid drop on a solid surface is shown and is established the independence of the dynamic contact angle on the interface width. In addition, the dependence of the dynamic contact angle on the Capillary number is matched with experimental data. Next, some generic sintering-like flows with a fixed matrix is presented. Different geometries in 2D and 3D are considered. We observed rapid wetting, precursor films, coalescence, breakup of melt drops as well as pore migration and elimination that are all microstructural characteristics of a liquid phase sintering. Finally, the effect of equilibrium contact angles on imbibition of liquid into a porous medium is studied.

Keywords: Capillary-driven flow; Wetting; Cahn–Hilliard/Navier–Stokes system; Sintering; Imbibition

---

1. Introduction

Capillary-driven flows involve two immiscible liquids or a liquid and air separated by a deformable interface in which the dynamics of the interface is largely influenced by capillary forces. A contact of these fluids with a third phase, usually a solid surface, gives rise to a phenomenon called wetting. The wetting phenomenon is pertinent to numerous processes such as penetration of liquids into porous rock, rise of sap in plants, and many others. The goal of this paper is to investigate numerically the wetting phenomenon in liquid phase sintering and in the imbibition of liquids into a porous medium.

Liquid phase sintering is a technological process that combines a particulate solid and a softer powder that acts as a binder, melts at a lower temperature and enhances material movement during the sintering

---

* Corresponding author. Tel.: +46 8 790 6871; fax: +46 8 796 9850.
E-mail addresses: walter@mech.kth.se (W. Villanueva), gustava@mech.kth.se (G. Amberg).

0301-9322/$ - see front matter © 2006 Elsevier Ltd. All rights reserved.
doi:10.1016/j.ijmultiphaseflow.2006.05.003

process. One of the oldest and most successful liquid phase systems is a cemented tungsten carbide with cobalt additive used for cutting and machining tools. Tungsten carbide is known to be hard and brittle while cobalt is relatively soft and ductile. The two metal powders which has typical fine grade sizes of about 1–10 μm in diameter are mixed and pressed, then heated until the cobalt binder melts. The liquid cobalt wets the solid grains and due to capillary forces, the microstructure undergoes rearrangement. Simultaneously, mass diffusion is present as well as grain growth that all contribute to pore elimination leading to densification. Some important factors influence the densification of the compact microstructure such as the amount of liquid present, particle size, solubility of the solid in liquid, contact angle, dihedral angle, etc. (German, 1985).

Wettability is the most significant phenomenon in liquid phase sintering, as stressed out by German (1985) and in experiments carried out by Motta et al. (2004) and Taguchi et al. (2004). However, this area has not been explored much using simulations. Some factors affecting wettability include contact angle, particle size, particle shape, and particle arrangement.

The wetting of a liquid on a solid can be characterized into two types: total wetting, when the liquid spreads completely; and partial wetting, when the liquid at equilibrium rests on the solid with a contact angle θ_e (de Gennes et al., 2004). Both are characterized by the spreading parameter $S = \sigma_{SO} - (\sigma_{SL} + \sigma)$ where the σ's are surface tensions at the solid/air, solid/liquid, liquid/air interfaces, respectively. $S > 0$ corresponds to total wetting and $S < 0$ corresponds to partial wetting. High-energy surfaces such as metallic surfaces has higher σ_{SO} values, thus increases S, compared to low-energy surfaces like plastics. Wettability can also be controlled through surface roughness and surface coatings. Surface roughness enhances wetting when the surface is hydrophilic and the opposite if the surface is hydrophobic.

The wetting phenomena can be viewed as a free interface problem where the interface between the two immiscible fluids are deformable and free to change their shape in order to minimize their surface energy. The problem can be modeled with sharp interface or diffuse-interface methods. Diffuse-interface methods consider the interface between the two fluids to have a non-zero thickness endowed with physical properties such as surface tension. For a review of the development of diffuse-interface models applied to different interfacial phenomena, see Anderson et al. (1998). Phase-field models are particular type of diffuse-interface models that are based on fluid free energy, an idea that can be traced to van der Waals (1893). One notable feature of such models is that the force singularity arising in the classical model of moving contact lines as pointed out by Huh and Scriven (1971) is no longer present due to mass transfer across the interface, for details see Seppecher (1996). Moving contact line dynamics has also been studied computationally by Jacqmin (1999) using the coupled Cahn–Hilliard/Navier–Stokes system. The convective Cahn–Hilliard equation is a continuum model of phase separation in a binary mixture. The equation takes into account creation, evolution, and dissolution of interfaces. The interface evolves through convection or diffusion driven by chemical potential gradients.

In Section 2, we formulate the Cahn–Hilliard equation with the boundary conditions followed by the Navier–Stokes equations for the fluid motion. Then a dimensionless system is derived and dimensionless parameters are identified. A numerical treatment of the system of equations is discussed. The results starting from a basic wetting phenomena of a liquid drop on a solid surface is shown in Section 3. We first establish the independence of the wetting contact angle on interface width. Wettability on different matrix of solid particles is presented. We observe that the particle size, shape, and arrangement of the solid particles has an effect in the densification of the compact microstructure. Finally, the effect of the equilibrium contact angle on wettability is considered. We will show that the smaller the contact angle the more liquid is imbibed into the porous medium leading to higher densification.

2. Mathematical formulation

2.1. The phase-field method

Consider the case of an isothermal, viscous, incompressible binary fluid consisting of two components, A and B. We can introduce an order parameter, a phase-field C, to characterize the two different phases and is analogous to the relative concentration between the two. In each bulk phases, C assumes a distinct constant value and changes rapidly but smoothly in the interfacial region. For example, component A assumes the value $C_A = -1$ while component B takes the value $C_B = 1$ and the transition from C_A to C_B describes the interfacial region. van der Waals (1893) modeled the system by introducing a free energy density f of the form:

$$f = \frac{1}{2}\alpha(\nabla C)^2 + \beta\Psi(C) \tag{1}$$

that is the sum of the gradient energy $\frac{1}{2}\alpha(\nabla C)^2$ and the bulk energy $\beta\Psi(C)$. The function Ψ is a double-well positive function that has two minima corresponding to the two stable phases. A simple example of such function is $(C+1)^2(C-1)^2$ which has minima at $C_{A,B} = \pm 1$ and a peak of high energy at $C = 0$. The constant parameters α and β are used to control the surface tension and the interface thickness which will be shown later.

Equilibrium interface profiles can be obtained by minimizing the free energy $\mathscr{F} = \int f \, dV$. The chemical potential, ϕ, of the liquid mixture is the rate of change of $\mathscr{F}$ with respect to C

$$\phi = \frac{\delta\mathscr{F}}{\delta C} = \beta\Psi'(C) - \alpha\nabla^2 C. \tag{2}$$

The equilibrium profiles are the solutions of the equation $\phi = \beta\Psi'(C) - \alpha\nabla^2 C \equiv$ constant. Two stable uniform solutions exist, $C_{A,B} = \pm 1$, that corresponds to the two bulk phases and a one-dimensional (say, along the x-direction) nonuniform solution exists and was first obtained by van der Waals (1893),

$$C_0(x) = \tanh\left(\frac{x}{\sqrt{2}\xi}\right), \tag{3}$$

where $\xi = \sqrt{\alpha/\beta}$ is the mean-field thickness. The equilibrium interface thickness ϵ is defined to be the distance from $C = -0.9$ to $C = 0.9$ and this width contains 98.5% of the surface tension stress (Jacqmin, 2000). With Eq. (3), $\epsilon = 2\sqrt{2}\xi\tanh^{-1}(0.9) = 4.164\xi$. The equilibrium surface tension σ of a plane interface can be found by integrating the free energy density along the interface,

$$\sigma = \alpha\int_{-\infty}^{\infty}\left(\frac{dC_0}{dx}\right)^2 dx = \frac{2\sqrt{2}}{3}\alpha^{1/2}\beta^{1/2}. \tag{4}$$

Note that the interface thickness ϵ and the surface tension σ can be controlled using the positive parameters α and β.

Cahn extended van der Waals model to time-dependent problems (Cahn, 1961) by approximating interfacial diffusion to be proportional to chemical potential gradients. The Cahn–Hilliard equation, modified to account for fluid motion is given by

$$\frac{\partial C}{\partial t} + (\mathbf{u}\cdot\nabla)C = \kappa\nabla^2\phi = \kappa\nabla^2(\beta\Psi'(C) - \alpha\nabla^2 C) \quad \text{in } \Omega, \tag{5}$$

where $\mathbf{u}$ is the velocity field and κ is the mobility. The Cahn–Hilliard equation models the creation, evolution, and dissolution of diffusively controlled phase-field interfaces (Bates and Fife, 1993).

Two boundary conditions are set for C. First, the no-flux condition

$$\mathbf{n}\cdot\nabla\phi = 0, \tag{6}$$

where $\mathbf{n}$ is the unit vector normal to the wall. Following Jacqmin (1999), the second boundary condition depends on the interface at the wall being at or near local equilibrium. The wall free energy is postulated to be of the form:

$$\mathscr{F}_w = \int \gamma g(C) dA, \tag{7}$$

where γ is the jump in solid/fluid surface energies from C_A to C_B. The function $g(C)$ is a local surface energy and is set to $0.75C$–$0.25C^3$ in this formulation. The resulting boundary condition is then

$$\alpha\mathbf{n}\cdot\nabla C + \gamma g'(C) = 0 \tag{8}$$

that corresponds to a diffusively controlled local equilibrium at the wall. We define the wetting coefficient k,

$$k = \frac{\sigma_{\mathrm{SO}} - \sigma_{\mathrm{SL}}}{\sigma} = \frac{S}{\sigma} + 1. \tag{9}$$

It can be shown that the normal gradient of the composition C is directly proportional to the wetting coefficient,

$$\mathbf{n} \cdot \nabla C = -\frac{k}{Cn} g'(C). \tag{10}$$

Cn is a dimensionless numerical parameter that will be discussed more in detail later.

We can also define the *Young's relation* (Probstein, 2003) which is only valid when $S < 0$,

$$\cos\theta_{\mathrm{e}} = k = \frac{S}{\sigma} + 1, \tag{11}$$

where θ_{e} is the static equilibrium angle taken to be the same as the dynamic contact angle right at the wall. Eq. (8) can also be extended to non-equilibrium situations by taking into account wall velocities.

2.2. The equations of fluid motion

The calculations in this paper are restricted to two phases having the same viscosity and mobility. The binary fluid motion is governed by the incompressible Navier–Stokes equations with phase-dependent surface tension forcing in its potential form, $-C\nabla\phi$,

$$\begin{aligned} &\rho_0\left(\frac{\partial \mathbf{u}}{\partial t} + (\mathbf{u}\cdot\nabla)\mathbf{u}\right) = -\nabla p + \mu\nabla^2\mathbf{u} - C\nabla\phi, \\ &\nabla\cdot\mathbf{u} = 0, \end{aligned} \tag{12}$$

where p enforces incompressibility and is related to the pressure, ρ_0 is the mean density, and μ is the viscosity. When the stress form of the surface tension force is used, p becomes the true pressure (Jacqmin, 1999).

2.3. Nondimensionalization

Define the dimensionless variables,

$$x' = \frac{x}{L_{\mathrm{c}}}, \quad u' = \frac{u}{U_{\mathrm{c}}}, \quad t' = \frac{tU_{\mathrm{c}}}{L_{\mathrm{c}}}, \quad p' = \frac{pL_{\mathrm{c}}}{\mu U_{\mathrm{c}}}, \tag{13}$$

where L_{c} is the characteristic length taken to be the domain size and U_{c} is the characteristic velocity. Dropping the primes, the dimensionless forms of Eqs. (5) and (12) are

$$\begin{aligned} &\frac{\partial C}{\partial t} + (\mathbf{u}\cdot\nabla)C = \frac{1}{Pe}\nabla^2\phi = \frac{1}{Pe}\nabla^2(\Psi'(C) - Cn^2\nabla^2 C), \\ &Re\left(\frac{\partial \mathbf{u}}{\partial t} + (\mathbf{u}\cdot\nabla)\mathbf{u}\right) = -\nabla p + \nabla^2\mathbf{u} - \frac{1}{Ca\cdot Cn}C\nabla\phi, \\ &\nabla\cdot\mathbf{u} = 0. \end{aligned} \tag{14}$$

The dimensionless physical parameters are the Reynolds number Re, Capillary number Ca, and Peclet number Pe given by

$$Re = \frac{\rho_0 U_{\mathrm{c}} L_{\mathrm{c}}}{\mu}, \quad Ca = \frac{2\sqrt{2}\mu U_{\mathrm{c}}}{3\sigma}, \quad Pe = \frac{2\sqrt{2}L_{\mathrm{c}}U_{\mathrm{c}}\xi}{3\kappa\sigma}. \tag{15}$$

The Reynolds number is the ratio between the inertial and viscous forces. The Capillary number gives the ratio between the viscous and surface tension forces. The bulk phase chemical diffusivity is given by $\xi^{-1}\sigma\kappa\Psi''(C_{\mathrm{A,B}})$. Accordingly, the Peclet number is the ratio between the convective and diffusive mass transport. The Cahn number $Cn = \xi/L_{\mathrm{c}}$ is a dimensionless numerical parameter that provides a measure of the ratio between the mean-field thickness ξ and the characteristic length L_c. For example, $Cn = 0.01$ means that for a 1 μm diameter droplet, the mean-field thickness is 0.01 μm. The choice of Cn is influenced, at least, by numerical accuracy, efficiency, and stability. Thick interfaces does not accurately describe the dynamics of the interface such as coalescences and breakups. Thin interfaces on the other hand reduces the length scale since the interface needs to be resolved. And for a flow problem, smaller length scale requires smaller time-step to achieve numerical stability and also given the fact that the Cahn–Hilliard equation has a biharmonic term which sets a severe time-step restriction. Moreover, without the use of mesh adaptivity, the small length scale is uniform all throughout the domain (assuming that interfacial dynamics almost covers the whole domain) thereby increasing the number of mesh points significantly which requires much longer computation time. In this paper, we consider capillary-driven laminar flows, so our values for the Reynolds number Re and Capillary number Ca are both small. We also consider problems where the convective mass transport is much higher than the diffusive mass transport, so the Peclet number Pe chosen is large.

It is important to note that the convective Cahn–Hilliard equation conserves mass. Using the divergence theorem in Eq. (14a) integrated over the domain Ω we have

$$\int_{\Omega} C_t \,\mathrm{d}x + \int_{\partial\Omega} (n \cdot \mathbf{u}) C \,\mathrm{d}S = \frac{1}{Pe} \int_{\partial\Omega} n \cdot \nabla\phi \,\mathrm{d}S. \tag{16}$$

And given that $n \cdot \mathbf{u} = 0$ and $n \cdot \nabla\phi = 0$,

$$0 = \int_{\Omega} C_t \,\mathrm{d}x = \frac{1}{\mathrm{d}t} \int_{\Omega} C(x) \mathrm{d}x \tag{17}$$

which implies that the rate of change of the composition C with respect to time over the entire domain is zero.

2.4. Numerical treatment

The numerical simulations were carried out using FemLego (Amberg et al., 1999), a symbolic tool to solve partial differential equations with adaptive finite element method. The partial differential equations, boundary conditions, initial conditions, and the method of solving each equation are all specified in a Maple worksheet (www.maplesoft.com). The Cahn–Hilliard equation is treated as a system where the chemical potential ϕ is computed first followed by the composition C (see Eq. (14a)) in which the right hand side of the equation is the Laplacian of the chemical potential. Both chemical potential and composition equations are discretised in space using piecewise linear functions. Moreover, an explicit Euler scheme is used to discretise the composition equation in time. The resulting linear systems of both equations are solved using conjugate gradient method. Since the model requires the interface to be resolved with at least 3-node points, the use of adaptivity is essential. An ad hoc error criterion is used to ensure mesh resolution along the vicinity of the interface (see Fig. 1c). The mesh adaptivity is implemented as follows: at each mesh refinement step, an element K is marked for refinement if the element size $h > h_{\min}$ (the minimum h allowed), and does not satisfy the following the error criterion:

$$\|H(a - |C(x,t)|)\|_{L^1(K)} \leqslant \mathrm{TOL}, \tag{18}$$

where $H(\cdot)$ is the Heaviside step function, a is a constant (here we used $a = 0.99$), and TOL is a given tolerance. If an element satisfies the error criterion, it is marked for derefinement unless it is an original element. At the next refinement step, elements containing hanging nodes are marked for refinement. The refinement/derefinement stops if and only if no element is marked for refinement/derefinement. The interface moves quite slow so the adaptivity is implemented at every 10th to 20th time-step.

The Navier–Stokes equations are solved using a projection method by Guermond and Quartapelle (1995) with an added pressure stabilization term. The Navier–Stokes equations are also discretised in space using piecewise linear functions and the linear systems are solved using conjugate gradient method. Typical mesh size in 2D with the mesh adaptivity ranges from 2000 to 6000 nodes depending on the dynamics of the interface. The 2D simulation on a single Linux PC takes between 5 and 10 h or more depending on the choice of parameters and extent of computation but with the average of 166 time-steps/min. In the 3D simulation, the number of nodes and elements increases dramatically so the use of parallel adaptive computation is necessary.

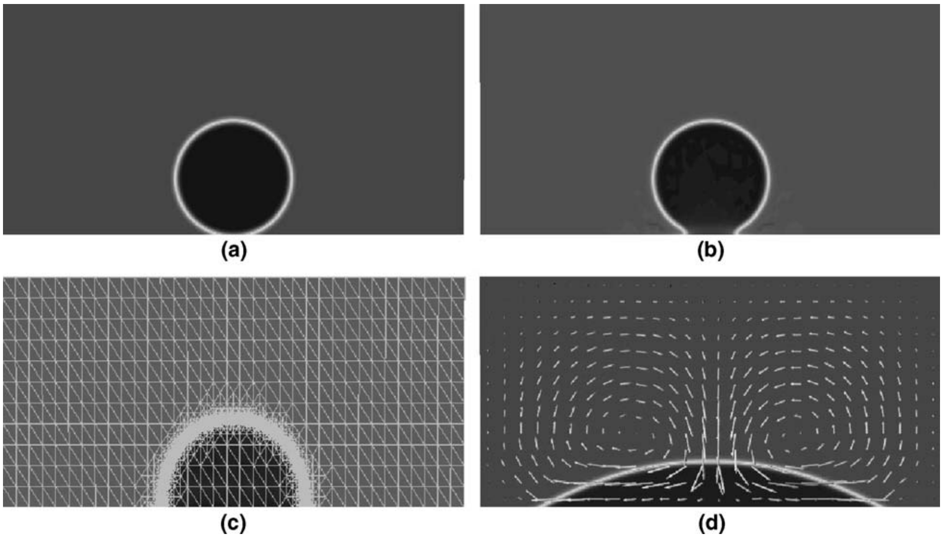

Fig. 1. Wetting of a liquid droplet on a solid surface. Concentration field at nondimensional time $t = 0, 1, 10, 200$ with $Ca = 1.0$, $Re = 1.0$, $Pe = 1.5 \times 10^4$, $Cn = 0.01$ and $k = 0.9063$ ($\theta_e \approx 25°$). The mesh and velocity field are superimposed in (c) and (d), respectively.

An extended version of FemLego that run on distributed memory has been used (Do-Quang et al., submitted for publication). The 3D computation was done on a Linux PC-cluster with 16 processors. Until the final time considered which is about 22,000 time-steps with a million elements and 200,000 nodes, the computation took about 52 h with seven equations to be solved or with a rate of 7 time-steps/min.

3. Results

We present wetting flows in different geometries. We start by showing a basic wetting phenomena of a liquid drop on a solid surface and show that the dynamic contact angle is fairly independent of the interface width. Next, some generic sintering flows with a fixed matrix will be shown where coalescence and breakup can be observed. The effect of particle size, shape, and arrangement to wettability is also discussed. And finally, we study the effect of static contact angles to impregnation or imbibition. We find that the smaller the contact angle the more liquid is imbibed into the porous medium leading to higher densification. In all simulations, we neglect the effect of gravity and consider only capillary effects as the driving force in the fluid motion.

3.1. Basic wetting phenomena

First, consider a 2D drop lying on a solid surface, see Fig. 1a with $Ca = 1.0$, $Re = 1.0$, $Pe = 10^4$, and $Cn = 0.01$. The wetting coefficient is $k = 0.9063$ and using Eq. (9), $S < 0$, thus we have partial wetting and the equilibrium contact angle is $\theta_e \approx 25°$. The drop is surrounded by another liquid with density similar to the drop. Consequently, the capillary length which can be estimated by relating the Laplace pressure to the hydrostatic pressure, increases and gravity can be neglected. Thus the liquid is considered to be in a zero-gravity environment where capillary effects dominate (de Gennes et al., 2004). In Fig. 1a, the drop is in contact with the surface at 158° apparent contact angle. Then the drop starts to spread and wets the surface, Fig. 1b, with a 141° apparent contact angle. In Fig. 1c, the drop spreads further with 77° apparent contact angle. The adaptive mesh is superimposed and shows fine resolution along the vicinity of the interface. Finally, the drop closely reaches the equilibrium contact angle of $\theta_e \approx 25°$ in Fig. 1d. The spreading is fast in the first stage and then slowly reach the equilibrium static contact angle. The velocity field is also superimposed and gives a symmetric profile with two vortices.

As mentioned earlier, the use of adaptivity is essential especially in larger systems since we need to resolve the interfaces. In this wetting case with $Cn = 0.01$, the minimum mesh spacing $h_{\min} = 0.0056$ and the number of nodes is between 3000 and 5000. After 10,000 time-steps, the computation time is 798 s with 3239 nodes at this point. Now, without adaptivity and keeping the same mesh spacing $h_{\min}$, the same domain gives 51,200 nodes. After 10,000 time-steps, the computation time is 14,261 s which is about 18 times slower than with adaptivity. Results at $t = 1$ of both with and without adaptivity are plotted in Fig. 2. In Fig. 2a, mesh adaptivity is implemented. This is a close up of Fig. 1b with the mesh. In Fig. 2b, mesh adaptivity is not implemented but the mesh spacing is the same as in the adaptive case. We get similar results for both. In Fig. 2c, mesh adaptivity is not implemented but with finer resolution than with the previous case and used 259,200 nodes requiring 86,679 s computation time. We get similar results in all cases which validates our adaptive scheme and the mesh resolution that has been used. The shape and position of the interface is very similar in all cases. The apparent contact angle is the same in all cases.

Conservation of mass is an important issue in modeling free interface problems. We require that the mass of the droplet is conserved, or at least the change is minimal and has a limit. Otherwise the droplet will either disappear or blow up which invalidates any measurement. We looked into the variation of the area of the 2D droplet from its initial value (Fig. 1). We found that the norm increases and reaches a value of about 1.0011 which means a slight increase of only 0.11% of the initial area. This is due to the reconfiguration of the interface from its initially set configuration to the stable configuration, that is, with an equilibrium interface profile given by Eq. (3) (tanh profile). The area remains constant after several time-steps.

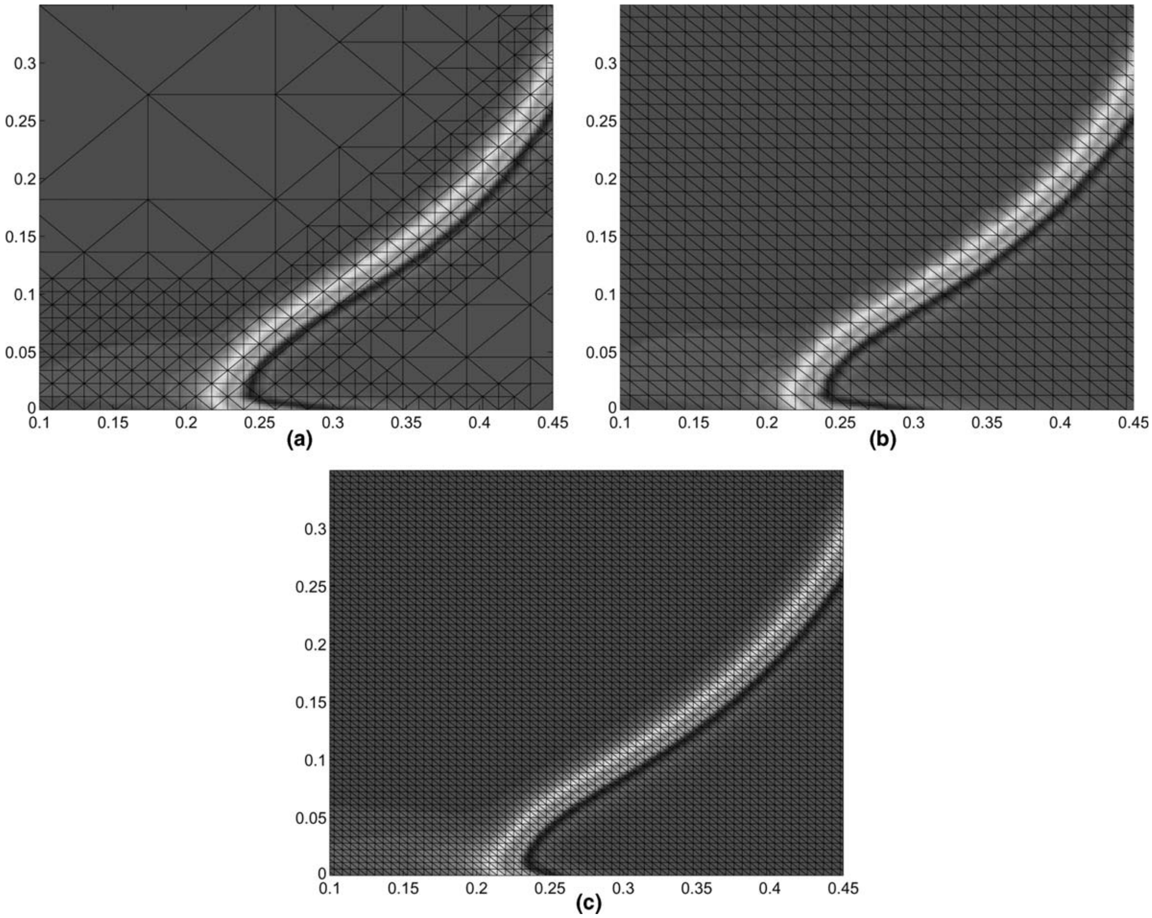

Fig. 2. Mesh adaptivity with $Cn = 0.01$ at $t = 1$: (a) with adaptivity and a total of 3239 nodes, plot is a close up of Fig. 1b, (b) without adaptivity and with the same mesh spacing as in the adaptive case gives 51,200 nodes, (c) without adaptivity and more refined mesh with 259,200 nodes. Similar results are obtained in all cases.

The apparent contact angle versus dimensionless time is plotted in Fig. 3. The figure suggests that the first stage of wetting is fast where the apparent contact angle decreases rapidly and then slows down upon reaching the equilibrium contact angle. In the final time considered, we measured an apparent contact angle of 26°, one degree higher than the theoretically set value of 25°. The apparent contact angle is also plotted versus the Capillary number for different interface thicknesses in Fig. 4. The apparent contact angle is fairly independent of the interface thickness. Moreover, the values taken on the dependence of the contact angle on the Capillary number is fairly close to the values taken experimentally by Hoffman (1975) using silicone oils. The values matched closer when the Capillary number approaches zero.

The values for *Cn* used for the computations in Fig. 3 were chosen to give interface widths less than relevant radii of curvature, while at the same time allowing reasonably quick results. The limited scatter that is present in Fig. 3 is attributed to uncertainites in determining the apparent contact angle. As demonstrated in Fig. 3, the increase or decrease of interface width by a factor of 2 has little consequence for the dependency of apparent contact angle on capillary number (or advancing speed). There is a fundamental reason for why this is

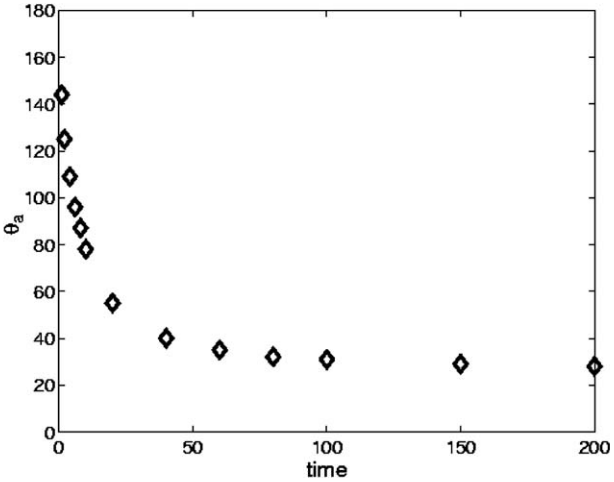

Fig. 3. Apparent contact angle versus dimensionless time for a liquid droplet.

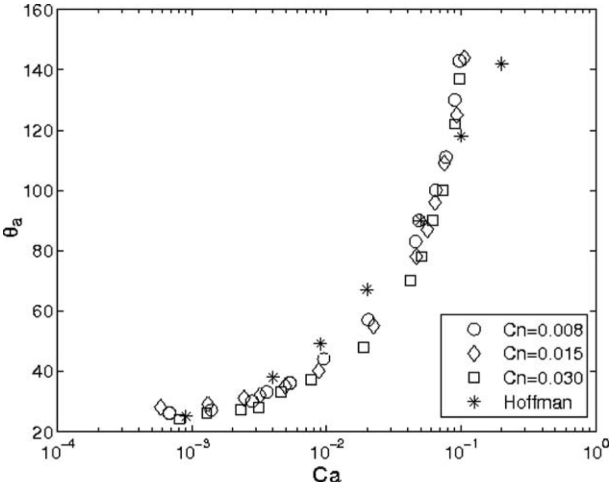

Fig. 4. Dependence of the contact angle on the Capillary number: (○), (◊), and (□) with different Cahn number *Cn* and (∗) with data from Hoffman's experiment using silicone oils (Hoffman, 1975).

expected, i.e., that the predicted dynamic wetting properties become independent of the interface width, when the interface width is less than the length scales for the interface geometry, i.e., the relevant radii of curvature.

In order to see this we will briefly discuss the fluid dynamics of the contact point, i.e., the fluid flow in a region of length scale interface width, around the apparent contact point. In the close up in Fig. 2 ($Cn = 0.01$), the contact point region would be an area of a cross-section of a few interface widths, say 0.05 around the apparent contact point. In this region the essential driving force for fluid motion is the capillary action on the highly curved interface near the wall, where the apparent contact angle is adjusted to the static one (which must always hold right at the wall). This change happens over the length scale of the interface width, which thus also sets the local radius of curvature. This corresponds thus to a driving pressure of the order (surface tension)/(interface width).

The flow resistance (assuming this to be small enough that a local Reynolds number is less than unity) scales with the viscous friction corresponding to a finite flow speed at one interface width from the wall. The flow resistance that balances the driving force is thus (viscosity)(speed)/(interface width). Both the driving force and the flow resistance are thus inversely proportional to the interface width, and the value of this will cancel, and not influence the result. Expressed differently we could say that the contact region is self similar, and that the actual value of the length scale of the region will not influence the resulting speed. Furthermore, we expect the Cahn–Hilliard system to describe the correct physics on length scales corresponding to real interface widths. Since we also observe above that the predicted dynamic wetting does not depend on the length scale as such, it is not surprising that good results can be obtained also with interfaces that are much thicker than the physical ones.

3.2. Some sintering-like flows

In this section, we show some examples of sintering-like flows. The binder powders are modeled with drops that melts and spreads through the solid grains, see Figs. 5 and 6. However, with the present model, the solid grains are rendered immobile. Nevertheless, the model captures qualitatively the most important phenomenon in liquid phase sintering which is wettability and how this is affected by contact angle, particle size and shape, and particle arrangement. The model also captures important microstructural behaviors in liquid phase sintering such as phase deformation, coalescence, breakup, pore migration, and pore elimination. In the simulations that follow, we observe coalescence through the collision of precursor films. Precursor films spread faster than the bulk fluid and feel no bounds unless the property of the surface changes in which S changes sign, or the film collides with another fluid of the same phase that initiates coalescence. Coalescence also occurs when two droplets collide and the separation length between the interfaces falls below a critical value. Experimentally, the critical length cannot be measured directly but the length is known to be comparable to the distance where van der Waals forces become important.

Fig. 5a shows nine liquid drops distributed over a fixed matrix of six solid particles with irregular shapes and sizes. The sizes of the drops are smaller than the solid particles. The parameters used are $Ca = 1.0$, $Re = 10$, $Pe = 10^5$, and $Cn = 0.01$. The wetting coefficient is $k = 1$ which corresponds to $S = 0$, a wetting transition. In this case, the equilibrium contact angle $\theta_e = 0°$. The droplets melt and rapidly wet the surface of the solid grains, and eight pores are formed (Fig. 5b). The melted drops continue to spread forming precursor films and coalesce with other droplets (Fig. 5c). The pores move towards the center of the compact and combine with other pores. The lower portion of the compact shows the breakup of a liquid melt when two pores are joining (Fig. 5c and d). Since we are dealing with two-phase flow, this is a situation where the coalescence of one phase is the breakup of the other. At this point, the dynamics of the compact slows down. Pores continue to move initiating coalescence, then subsequently shrink and disappear due to diffusion which is the dominating process at this later stage (Fig. 5e and f).

A different matrix of solid grains is used in Fig. 6 with the same physical parameters. In Fig. 6a, droplets are combined with grains of same shapes and sizes and arranged uniformly. In this case the solid grains are modeled with squares and the droplets with circles. The drops when melted then start to spread and wet the solid grains, see Fig. 6b. Coalescence takes place and pores are formed. Precursor films developed (which are evident in Fig. 6c) and are the result of having a zero static contact angle. In this example, no pores disappeared until the final time considered and no significant change can be observed from Fig. 6c and d.

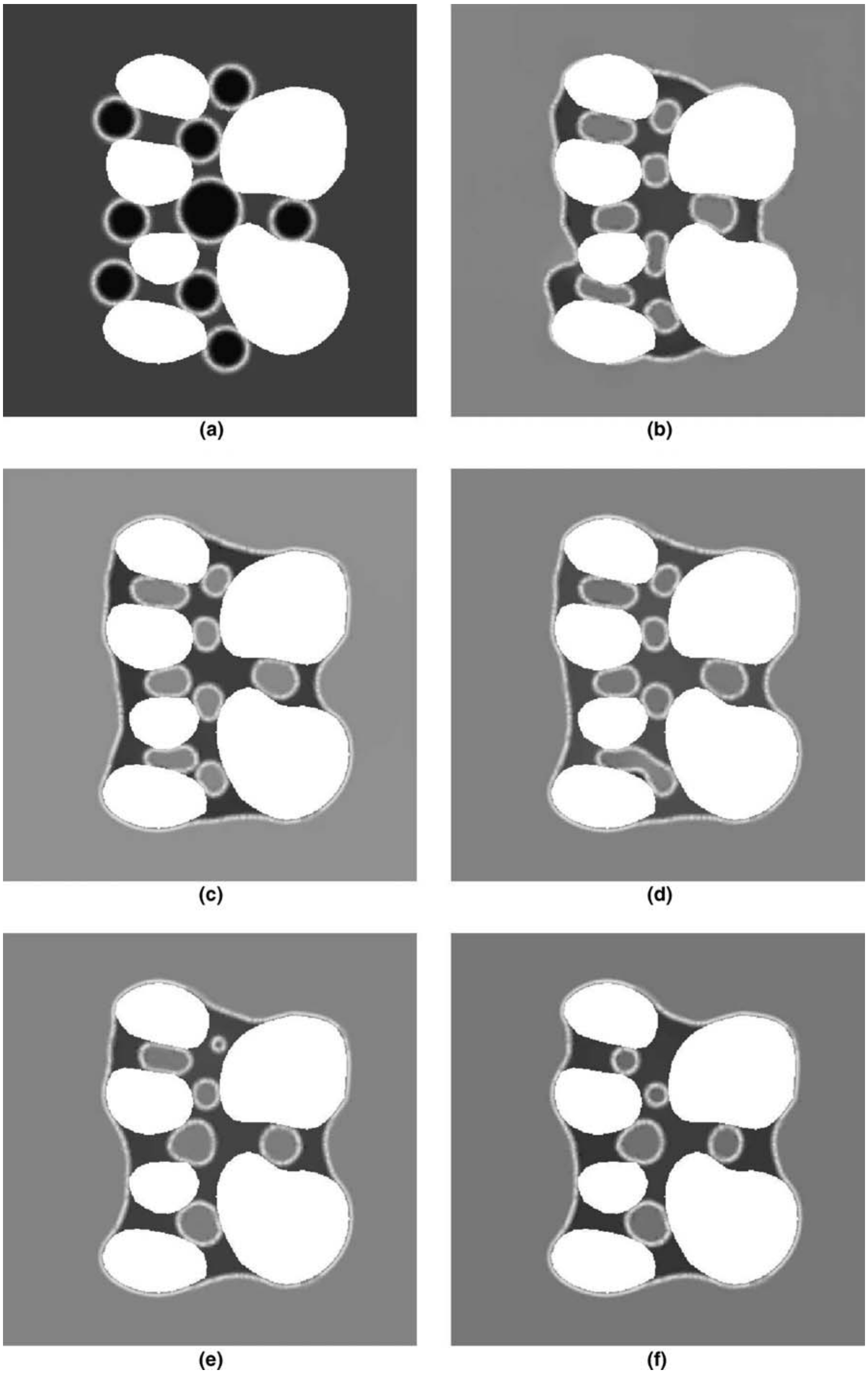

Fig. 5. Generic sintering flow with a fixed matrix of solid particles of irregular shapes and sizes. Concentration field at $t = 0, 2, 16, 18, 220, 500$ with $Ca = 1.0$, $Re = 10$, $Pe = 10^5$, $Cn = 0.01$, and $k = 1$.

The average velocity of both cases with square and irregular particles are plotted in Fig. 7. The case with square particles starts from 0 and reaches 0.237 at $t = 1$ then rapidly drops to 0.1 level until $t = 18$. The rapid increase in velocity is due to fast wetting and rapid change in the configuration of the pores from irregular to circular shapes which is a consequence of the minimization of the free energy. The 0.1 level corresponds to spreading of the precursor films and further reconfiguration of the pores. After this stage, the dynamics of

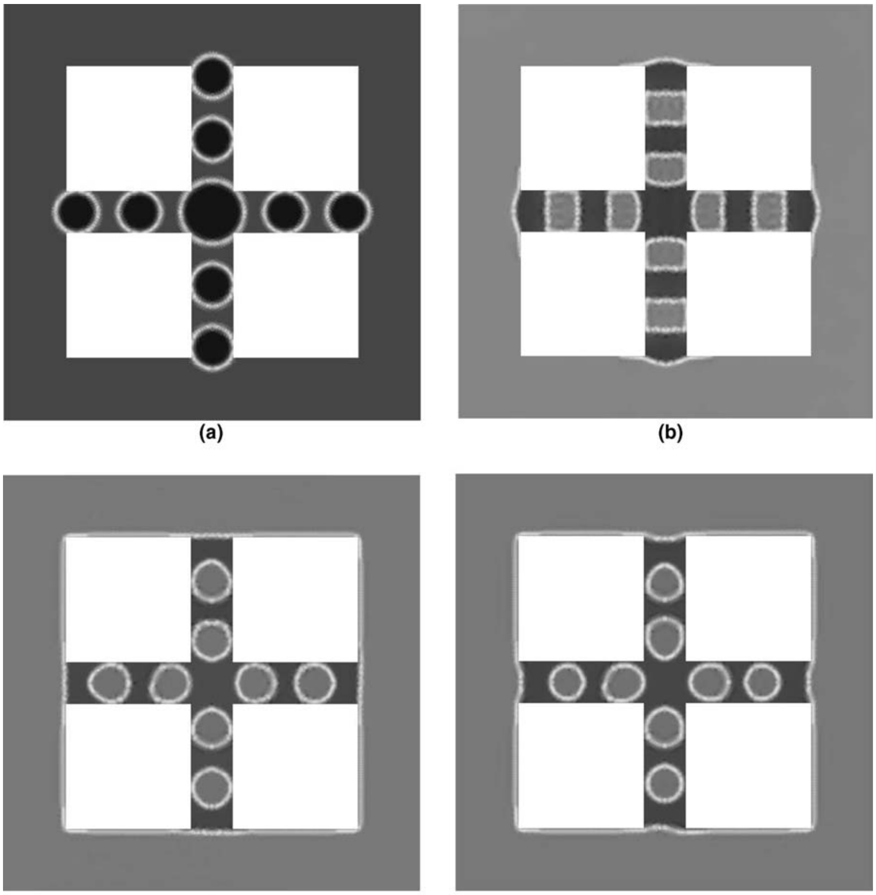
(a) (b) (c) (d)

Fig. 6. Generic sintering flow with a fixed matrix of solid particles of same shapes and sizes. Concentration field at $t = 0, 1, 20, 200$ with $Ca = 1.0$, $Re = 10$, $Pe = 10^5$, $Cn = 0.01$, and $k = 1$.

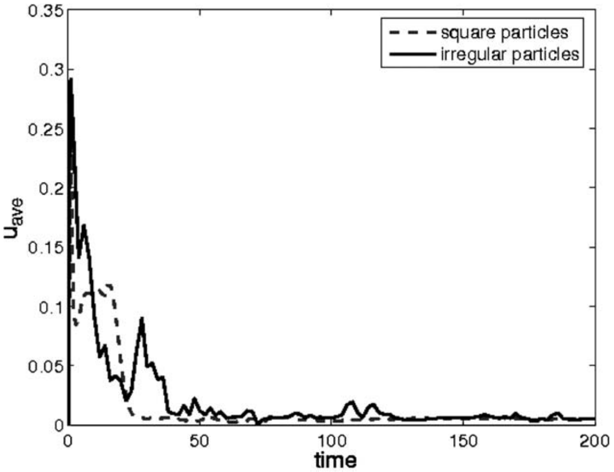

Fig. 7. Average velocity versus dimensionless time of two different matrix of solid particles.

the microstructure slows down and the diffusion process dominates in which the average velocity decreases upto two orders of magnitude. The case with irregular shape particles gives a slightly different behavior.

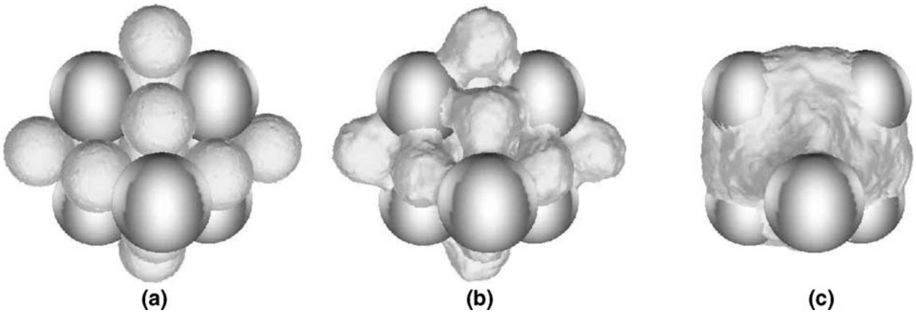

Fig. 8. Three-dimensional generic sintering with a fixed matrix of solid particles (larger spheres). Isosurface at $t = 0, 2, 11$ with $Ca = 0.1$, $Re = 0.1$ and $Pe = 10^4$.

The average velocity rapidly increases to 0.292 which is higher than the previous case and this rapid increase is also attributed to fast wetting and pore filling that results to rapid change in the configuration of the pores from irregular to circular shapes. The second peak in the average velocity is due to coalescences of pores and reconfiguration of the resulting pore into a circular shape (see Fig. 5d). Similar to the previous case, the dynamics of the compact slows down with diffusion process starting to dominate that aids in pore elimination. Even without rearrangement in our model, the rapid increase and decrease in velocity is consistent with the actual liquid phase sintering process where the first stage is considered to be fast and the second to be very much slower.

An extension of the 2D generic sintering in 3D is shown in Fig. 8. The compact microstructure consists of six solid particles (larger spheres) and 13 melt drops that are evenly distributed. The drops melt and spread over the solid grains. Similar to the 2D case, coalescence, pore migration and elimination take place.

3.3. Imbibition

In this section, we look into the effect of equilibrium contact angle on wetting. Fig. 9a shows a fixed matrix of solid particles which can be thought of as a porous medium partially submerged in a pool of liquid. The no-slip boundary condition is used on the left and right edges of the domain including the inner edges while the top and lower edges allow fluid to pass through, i.e., fluid gets in from below and the other fluid is pushed out of the domain. The parameters used in this case are $Ca = 1.0$, $Re = 0.1$, $Pe = 10^5$, and the wetting coefficient $k = 1$ or $\theta_e = 0°$. With a zero equilibrium contact angle the liquid rapidly spreads over the surface of the solid grains forming precursor films (Fig. 9b). In reality, precursor films have thickness comparable to the thickness of the interface and can be detected by electrical means (de Gennes, 1992). The liquid continues to spread and a bulk of liquid is drawn into the porous medium (Fig. 9c and d).

For the case with a higher equilibrium contact angle, $\theta_e = 60°$, the wetting behavior is quite different as can be seen in Fig. 10. In Fig. 10a, a porous medium has its end dip into a pool of liquid. The parameters used is the same as in the previous case, $Ca = 1.0$, $Re = 0.1$, $Pe = 10^5$. The liquid starts to spread and wet the surface of the solid grains but no precursor films can be observed unlike in the previous case. Due to capillary forces, the liquid continues to penetrate into the porous medium (Fig. 10c and d). The interface tries to find its equilibrium state, that is, the profile that minimizes the free energy of the system. In Fig. 10c, there are three channels in the lower part of the medium and two of them located on the sides have similar shapes which narrows up while the one in the middle broadens. We observed from Fig. 10d that the liquid in the two side channels rise up higher than the one in the middle. Actually, the liquid in the middle channel only risen up a bit and one end of the interface got stuck at a corner of the middle channel.

The amount of liquid that is imbibed into the porous medium with respect to time is plotted in Fig. 11 for the two cases. The case with $\theta_e = 0°$ draws in more liquid than with $\theta_e = 60°$ which implies that the lower the contact angle the better the wettability of the system. In both cases, the advancement of the liquid starts out rapidly and then subsequently slows down.

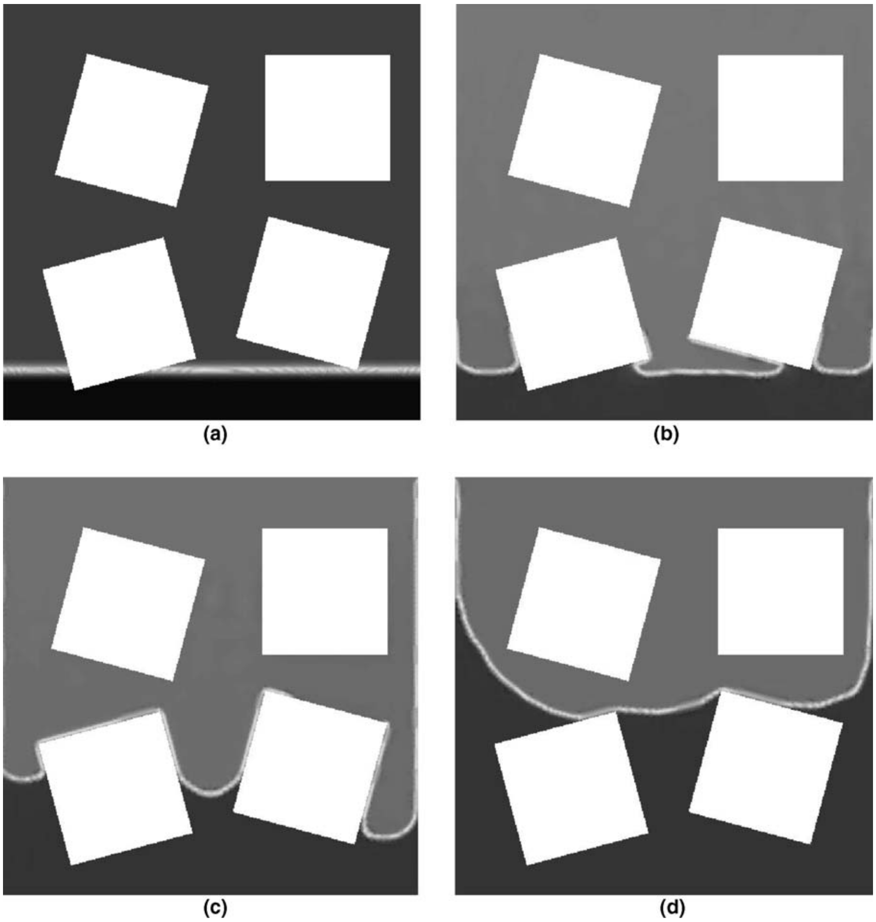

Fig. 9. Imbibition of a liquid into a porous medium. Concentration field at $t = 0, 2, 40, 500$ with $Ca = 1.0$, $Re = 0.1$, $Pe = 10^5$, $Cn = 0.01$, and $\theta_e = 0°$.

Darcy's law is a macroscopic description of flow in porous media in the presence of gravity. It relates the volumetric flow rate to the pressure gradients, bulk viscosity, and permeability (Batchelor, 1967). It was derived from simplifications made to the Navier–Stokes equations and is only valid for slow and viscous flow. It does not describe microscopically the movement of liquid fronts, specifically, how it behaves given a wetting condition and geometrical configuration of the system, i.e., particle size and shape, particle arrangement, and roughness. A more specific description of how liquid fronts move in a column, or simply put, in the presence of gravity, a fluid with density ρ rises at a height H in a column of radius R that is given by the Jurin's height (de Gennes, 1992), $H = 2\sigma\cos\theta_e/\rho g R$. Note the dependence of the height to the equilibrium contact angle. This is only valid, however, when the radius of the capillary is much smaller than its height. Moreover, this law takes into account cylindrical geometries or two parallel plates close to each other (with some modification to the constant factor) but not converging or diverging tubes or plates. In many porous media, they have complicated structure and connectivity of pores, as well as roughness which significantly affects the wetting condition of the system especially with microstructural systems. In general, liquid fronts tries to find its equilibrium state that is the state where the free energy is minimum. In a channel that narrows up with $0 < \theta_e < 90°$ and neglecting the effect of gravity, the liquid will rise up to the top because it minimizes the free energy by doing so unlike in a channel that broadens up, it requires more energy to rise up since it has to increase its surface area, just like what we observe in Fig. 10. For $\theta_e = 0$ in the absence of gravity, the liquid rises or penetrates the channel to its end without any regard of the channel's topological structure.

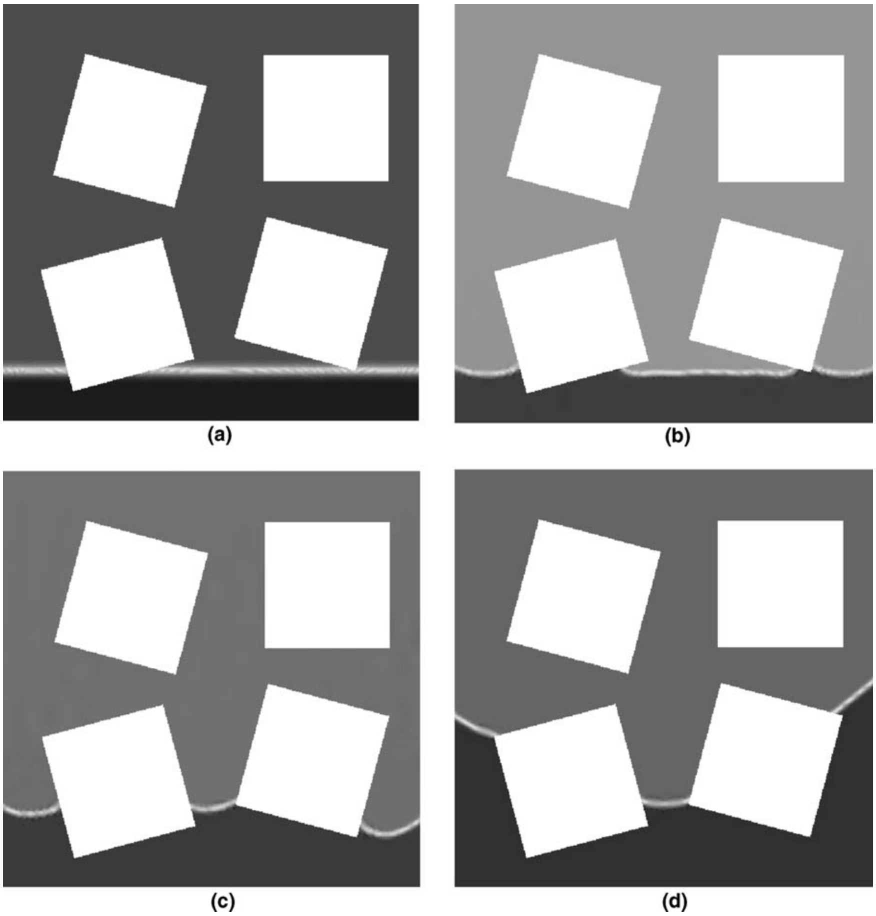

Fig. 10. Imbibition of a liquid into a porous medium. Concentration field at $t = 0, 2, 40, 500$ with $Ca = 1.0$, $Re = 0.1$, $Pe = 10^5$, $Cn = 0.01$, and $\theta_e = 60°$.

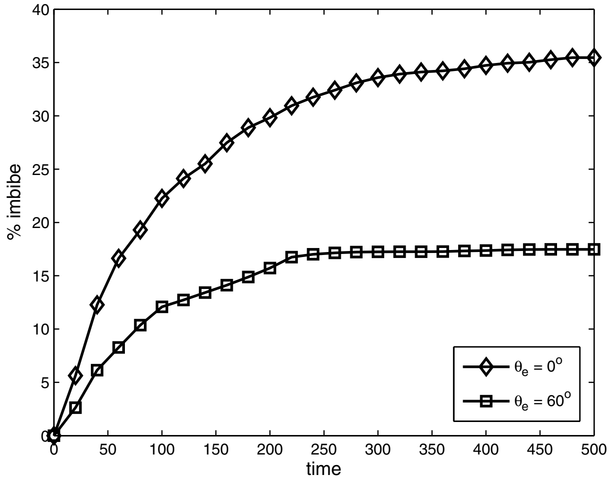

Fig. 11. Effect of equilibrium contact angle to imbibition of liquid into a porous medium.

4. Conclusion

We have investigated numerically the wetting phenomena in some capillary-driven flows. First, we showed a basic wetting phenomenon of a liquid drop on a solid surface and established the independence of the dynamic contact angle on the interface width. The values taken on the dependence of the contact angle on the Capillary number was compared with experimental values and they are in good agreement especially when the Capillary number approaches 0. We also presented successful simulations of some generic sintering flows with a fixed matrix in 2D and 3D. The model captured qualitatively the most important phenomenon in liquid phase sintering which is wettability. We have also investigated how wettability is affected by contact angle, particle size and shape, and particle arrangement. Interestingly, the model also captured important micro-structural behaviors in liquid phase sintering such as phase deformation, coalescence, breakup, pore migration, and pore elimination. Finally, the effect of equilibrium contact angles on imbibition of liquid into porous medium is studied. We found that the smaller the equilibrium contact angle the more liquid is imbibe into the porous medium. In addition, the structure of the channel also affects the imbibition of liquid.

The next step of our simulation is to allow the solid particles to move. In that case, the model has to be extended by adding one stiff phase-field variable that corresponds to the solid particles with the ability to coarsen, also called Ostwald ripening. In addition, our representation of the interface is too thick, giving us only a qualitative picture of the coalescences and breakups. A molecular dynamics simulation of the interaction between the molecules of the different phases can be coupled with the present model to give a more accurate description of the coalescence and breakup of the melt. Moreover, a molecular dynamics simulation can also supply input parameters in the present model such as the wetting coefficient $k(t)$ of the given system and the surface tension σ of the fluid interface in cases where no experimental data are available for the system under investigation.

Acknowledgements

The authors gratefully appreciate the valuable discussions with the members of the Computational Phase Transformation Research Group, KTH. This work was financially supported by the Swedish Foundation for Strategic Research (SSF).

References

Amberg, G., Tönhardt, R., Winkler, C., 1999. Finite element simulations using symbolic computing. Math. Comput. Simulat. 49, 257–274.

Anderson, D.M., McFadden, G.B., Wheeler, A.A., 1998. Diffuse-interface methods in fluid mechanics. Annu. Rev. Fluid Mech. 30, 139–165.

Batchelor, G.K., 1967. An Introduction to Fluid Dynamics. Cambridge University Press.

Bates, P.W., Fife, P.C., 1993. The dynamics of nucleation for the Cahn–Hilliard equation. SIAM J. Appl. Math. 53, 990–1008.

Cahn, J.W., 1961. On spinodal decomposition. Acta Metall. 9, 795–801.

de Gennes, P.G., 1992. Simple Views on Condensed Matter. World Scientific Publishing Co. Pte. Ltd.

de Gennes, P.G., Brochard-Wyart, F., Quéré, D., 2004. Capillarity and Wetting Phenomena. Springer-Verlag, Inc., NY.

Do-Quang, M., Singer-Loginova, I., Villanueva, W., Amberg, G., submitted for publication. Problem solving environment for parallel adaptive computation. Comput. Methods Appl. Mech. Engrg.

German, R., 1985. Liquid Phase Sintering. Plenum Press, NY.

Guermond, J.L., Quartapelle, L., 1995. Unconditionally stable finite-element method for the unsteady Navier–Stokes equations. In: Proc. Int. Conf. Finite Elements in Fluids, Venezia, 15–21 October.

Hoffman, R., 1975. A study of the advancing interface. J. Colloid Interface Sci. 50, 228–241.

Huh, C., Scriven, L.E., 1971. Hydrodynamic model of steady movement of a solid/liquid/fluid contact line. J. Colloid Interface Sci. 35, 85–101.

Jacqmin, D., 1999. Calculation of two-phase Navier–Stokes flows using phase-field modeling. J. Comput. Phys. 155, 96–127.

Jacqmin, D., 2000. Contact-line dynamics of a diffuse fluid interface. J. Fluid Mech. 402, 57–88.

Motta, F.V., Balestra, R.M., Ribeiro, S., Taguchi, S.P., 2004. Wetting behaviour of SiC ceramics, Part I. Mater. Lett. 58, 2805–2809.

Probstein, R.F., 2003. Physicochemical Hydrodynamics, An Introduction. John Wiley and Sons, Inc.

Seppecher, P., 1996. Moving contact lines in the Cahn–Hilliard theory. Int. J. Eng. Sci. 34, 977–992.

Taguchi, S.P., Motta, F.V., Balestra, R.M., Ribeiro, S., 2004. Wetting behaviour of SiC ceramics, Part II. Mater. Lett. 58, 2810–2814.

van der Waals, J.D., 1893. The thermodynamic theory of capillarity under the hypothesis of a continuous variation of density. Verhandel. Konink. Akad. Weten. 1 (J. Stat. Phys.) 20, 1979 (in English).